Applied Thermal Engineering 224 (2023) 119996

Contents lists available at ScienceDirect

Applied Thermal Engineering

journal homepage: www.elsevier.com/locate/ate

Design and commissioning of experiments for supersonic ORC nozzles in linear cascade configuration

Marco Manfredi, Giacomo Persico, Andrea Spinelli *, Paolo Gaetani, Vincenzo Dossena

Politecnico di Milano, Energy Department, Milano, 20156, Italy

ARTICLE INFO

Keywords:
Organic Rankine cycles
ORC turbine experiments
Linear turbine cascade design
CFD simulation of ORC cascade
Measurement techniques for non-ideal flows

ABSTRACT

In organic Rankine cycle (ORC) power systems, the turbo-expander involves the major technical challenges as the demand for compactness and flexibility of operation couples with severe compressibility and non-ideal gas effects. For these reasons the design of ORC turbines heavily relies on advanced aerodynamic models, whose validation is crucial but is still limited due to a lack of experimental data. To fill this gap, an experimental campaign on supersonic ORC nozzle cascades has been launched at Politecnico di Milano. This paper describes the conception and set-up of a novel class of experiments on linear cascades representative of stator nozzles of axial/radial ORC turbines, and aims at serving as a reference for future experimental investigations on ORC cascades. The paper also discusses the technical challenges of performing measurements on supersonic flows for a vapor at thermodynamic conditions close to saturation. Moreover, the paper reviews all steps required to design the campaign, discussing the blade design and the numerical simulations performed to assess the flow configuration in the linear cascade, with emphasis on the periodicity of the flow. The main objective of the experiments is to investigate the flow phenomena occurring in the blade trailing edge region and to retrieve the total pressure losses through the cascade with a relatively high spatial resolution, aiming at providing a benchmark for numerical simulations. To this end, the set of measurement techniques includes supersonic total pressure probes and wall pressure taps, as well as thermo-couples and schlieren visualizations. The main result of this preliminary work is the implementation of a relatively simple methodology to carry out experiments in blade cascade operated with organic vapors and aimed at evaluating cascade losses, without resorting to specifically calibrated instrumentation.

1. Introduction

The organic Rankine cycle (ORC) is a recognized solution to exploit renewable energy sources and to recover waste heat for power and combined heat and power production. ORCs implement a Rankine cycle with an organic fluid replacing water as working media. ORC effectiveness over competing technologies is indubitable in low-to-medium temperature range and power output. This is to be ascribed to the use of molecularly complex and high molecular mass compounds, whose choice allow to combine good cycle efficiency with plant simplicity and reliability [1,2]. Fig. 1 depicts in a temperature - specific entropy per unit mass ($T - s$) diagram a regenerative, supercritical organic Rankine cycle with siloxane MM (hexamethyldisiloxane, $C_6H_{18}OSi_2$) as working fluid. In the $0.1-10$ MW range ORC system are well established with worldwide spread installation, while in the few kW range they are considered as a promising solution, for instance to recover thermal energy from internal combustion engines (ICEs) on-board of innovative long-haul vehicles.

ORC expander architecture is strictly related to the system size and span from axial or radial outflow turbines for large power, to radial inflow turbine for mini and micro-ORC applications. Volumetric expanders are also employed for low power and especially low temperature applications. As it is well known, the expander represents a crucial component in organic Rankine cycle power systems and its efficiency strongly impacts on overall cycle performance and plant profitability [1,2]. Utmost attention is therefore usually payed to its fluid dynamic design and high-fidelity design/optimization tools based on computational fluid dynamics (CFD) are nowadays largely employed. However, during preliminary system design (involving fluid selection, cycle layout definition, specification of component architecture, as heat exchangers and fluid machines, and their initial sizing), the high computational effort typical of high-fidelity expander design tools prevent their integration in the overall optimization process, due to the considerable number of simulations initially required. A viable option to integrate the expander preliminary optimization within the

* Corresponding author.
E-mail address: andrea.spinelli@polimi.it (A. Spinelli).

https://doi.org/10.1016/j.applthermaleng.2023.119996
Received 22 February 2022; Received in revised form 14 December 2022; Accepted 3 January 2023
Available online 13 January 2023

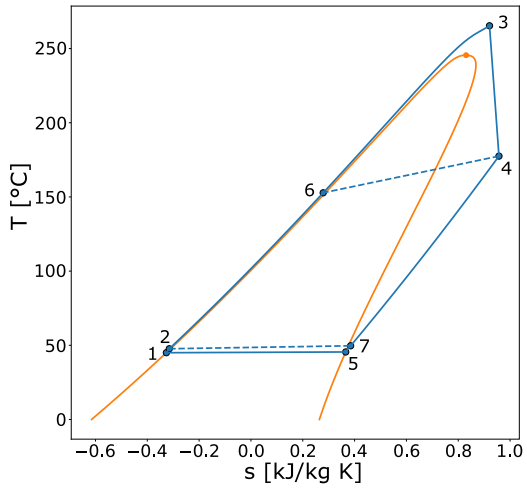

Fig. 1. Temperature - specific entropy per unit mass diagram representing a regenerative supercritical cycle (blue lines) implemented with siloxane MM. Process 3–4 is the vapor expansion occurring in the expander. Liquid-vapor saturation curve and the critical point are depicted in orange.

ORC system design consists in the adoption of reduced-order methods, capable of providing machine preliminary geometry, efficiency, and off-design performance with a reduced computational cost. Referring to turbo-expanders, preferred for high temperature/high expansion ratio ORCs and under study in the presented research, such tools are the so called mean-line methods [3–5]. These models and their results can be easily integrated, possibly in the form of look-up tables, within cycle optimization loops [6,7]. The capability and reliability of reduced-order models in correctly predicting turbine efficiency depend on the effectiveness and ranges of validity of the adopted loss correlations. Several loss models, spanning a wide range of empiricism level, are available in literature for both axial and radial turbine architectures [8–12]. The weakness of such relations is that they were developed for machines operating with conventional fluids and validated against test cases concerning standard gas or steam turbines, while their verification against experimental data over ORC expanders is largely lacking. An approach commonly adopted is to validate reduced-order models and loss correlations using high-fidelity CFD simulations [13,14]. However, the verification of CFD simulations relies only on the accuracy of state-of-the-art thermodynamic fluid models [15] or, at most, on experimental data related to paradigmatic compressible flows, such as isentropic nozzle expansions [16–18] or flows around aerodynamic [19] or bluff bodies [20], where loss impact on the flow field substantially differs from the case of turbine channel flows. The only exception is the work by [21], in which total pressure measurements were performed downstream of a micro supersonic annular cascade operated with air, carbon dioxide, and refrigerant R134a. In fact, the total pressure was measured downstream of the probe-induced shock, while the actual cascade-exit total pressure was retrieved numerically. Moreover, the measurement space resolution was limited by the miniaturization of the cascade. Finally, in the test conditions air and carbon dioxide exhibited an ideal-gas behavior, while only R134a showed mild non-ideal effects (minimum compressibility factor $Z = 0.88$, where Z quantifies the deviation of the fluid behavior from the ideal gas one and it is defined as $Z = P/\rho RT$, where P is the pressure, T the temperature, ρ the density and R the specific gas constant). As a result, the experiments documented in [21] were essentially devoted to evaluate the effect of fluid molecular complexity in wake losses. Therefore, experimental data concerning non-ideal and supersonic flows representative of ORC turbine cascades are still missing in the literature. By reproducing all the important features of these flows, namely the trailing-edge shock system, the wake generation and recovery, and the total pressure loss, such experiments would also be instrumental for constructing and validating high-fidelity CFD models implemented into ORC turbine design and analysis tools.

To this end, an experimental campaign has been designed at Politecnico di Milano on an ORC linear cascade, assembled within the Test Rig for Organic VApors (TROVA). The test section consists in a supersonic converging-diverging nozzle blade row, designed to operate at nominal outlet mach number of 1.6 (typical of highly loaded stages) with siloxane MM (hexamethyldisiloxane), a working fluid employed in high temperature ORCs. The fluid thermodynamic conditions envisaged for tests span from highly non-ideal states (inlet total pressure and temperature $P_T \approx 25$ bar, $T_T \approx 260$ °C, corresponding to compressibility factor as low as $Z \approx 0.3$) to dilute gas conditions. For CFD validation purposes, the evaluation of total pressure losses across the row is addressed as the experiment main objective. This in turn requires to measure total conditions P_T, T_T upstream and total pressure downstream the cascade. Schlieren visualization are also considered as a complementary technique to visualize fish tail shock pattern departing from blade trailing edge. The paper reports the full process of experiment design, which substantially differs from the case of conventional blade cascades (typically tested in cold-flow facilities using air at low temperature and pressure) due to challenging operating conditions and the need of complying with space constraints dictated by the test section geometry, while keeping at the same time the high spatial resolution needed for CFD validation. The design of experiment included blade shape definition and optimization in annular configuration, followed by their adaptation in planar cascade within the TROVA test section (including boundary walls) and structural verification. Also, instrument arrangement and traversing system were devised and designed. CFD simulations were largely employed for blade profile optimization in annular row; also the whole flow simulation of the final planar cascade was performed as the last step preceding the experiments, in order to assess the flow field to be measured and to verify the attained degree of periodicity.

2. Concept of the cascade experiment

With the aim of generating benchmark data, the experiment arrangement was conceived to match multiple requirements. Designing a cascade geometry representative of actual high-temperature and high-expansion ratio turbines was deemed key, as well as operating the blade row with a fluid and at thermodynamic conditions relevant for state-of-the-art and innovative high-temperature ORC power plants. Also, simplified solutions were devised for test section layout, instrument equipment, and for the test run procedure. Finally, the application of proven measurement techniques for organic vapors was envisaged.

The typically high value of the turbine stage expansion ratio, coupled with the low speed of sound of organic compounds, generally lead to supersonic flows at the first stator outlet. Therefore, a converging-diverging geometry was chosen as representative of ORC turbine nozzle. An illustrative sketch of the test section is reported in Fig. 2, while the design details are discussed in Sections 4.2–4.4. The cascade, constrained by the limited dimensions of the test section plate (red box in Fig. 2), features three complete blades, defining two central channels, together with two partial profiles at the boundaries of the domain, sketched for clarity (in gray). In the final cascade layout, the two partial profiles are replaced by side-walls (see Section 4.3 and Fig. 8), designed to improve flow periodicity and reduce shock disturbances at the measurement points. The blade profile of Fig. 2 is to be considered a baseline geometry, derived from an axial ORC stator investigated in [22] and adapted to the present experiment to obtain a linear cascade configuration. The baseline shape is optimized to minimize cascade entropy production, as described in Section 4.2. A stagger angle $\alpha_s = 75°$ (see Fig. 2) was selected for the cascade to be consistent with the application considered and to reduce, at the same time, the extent of the semi-bladed channel portion. This allows

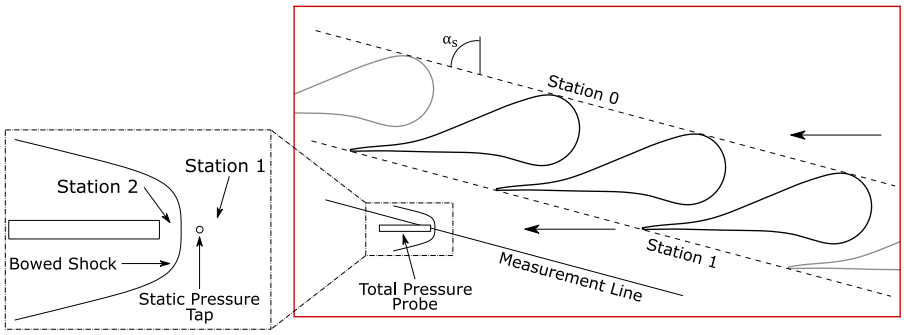

Fig. 2. Test section sketch.

to avoid a markedly stretched configuration, which would conflict with geometrical constraints of the test section, due to the choice of designing the row with inlet and outlet parallel flows (no flow deflection). This option not only notably simplifies the cascade assembly in the TROVA test section, but also turns out to be representative of radial inflow nozzles, which typically receive rather tangential flow from the volute and are characterized by camberlines with almost constant angle with respect to radial direction producing small flow deflections. Moreover, as proven in Section 4.2, this configuration is also relevant for axial turbine supersonic stators, which are mostly front-loaded, with flow turning (even remarkable) almost completed through the converging portion, while most of the entropy production occurs in the diverging part of the channel. Additionally, as long as supersonic flows are established, the flow rotation upstream the throat does not affect the downstream flow-field topology.

Total pressure is measured at both cascade inlet P_{T0} and outlet P_{T1}. As illustrated in the following, P_{T1} is retrieved by total pressure P_{T2} measured at the head of an overhung total pressure probe. As depicted in the detail of Fig. 2, a detached bowed shock sets up at total pressure probe head. Considering a flow-aligned probe, the shock is normal in front of the head tap. The total pressure P_{T2} measured by the probe is therefore the one established downstream the shock (station 2 in Fig. 2) which is lower than the value P_{T1} downstream the cascade, due to probe-induced shock losses. Being reasonable to assume an adiabatic flow within the test section, at least two additional quantities need to be concurrently measured to unambiguously retrieve P_{T1}, as clarified by systems of Eqs. (1), where, from left to right, the thermodynamic model of the fluid, the integral balance equations through an adiabatic normal shock, and the energy equation across sections 0–1 and 0–2 are specified.

$$\begin{cases} h_{T0} = h\left(T_{T0}, P_{T0}\right) \\ h_1 = h\left(\rho_1, P_1\right) \\ h_2 = h\left(\rho_2, P_2\right) \\ s_2 = s\left(\rho_2, P_2\right) \\ s_2 = s\left(h_{T2}, P_{T2}\right) \end{cases}, \quad \begin{cases} \rho_1 V_1 = \rho_2 V_2 \\ \rho_2 V_2^2 - \rho_1 V_1^2 = P_1 - P_2 \\ h_1 + \frac{V_1^2}{2} = h_2 + \frac{V_2^2}{2} \end{cases}, \quad \begin{cases} h_1 + \frac{V_1^2}{2} = h_{T0} \\ h_{T2} = h_{T0} \end{cases}. \tag{1}$$

In Eqs. (1), V_1 and V_2 represent, respectively, the velocity components upstream and downstream the normal portion of the bowed shock. Eq. (1) form a system of 10 mathematical relation in 12 unknowns, namely h_1, P_1, ρ_1, h_2, P_2, ρ_2, s_2, V_1, V_2, h_{T0}, h_{T2}, and T_{T0}, where h and s stand for specific enthalpy and entropy per unit mass respectively. Subscript T refers to total conditions and subscripts 0, 1, and 2 specify respectively section upstream/downstream the blade row and downstream the probe-induced shock. To attain a well-posed mathematical problem, two independent additional quantities are required, namely the inlet total temperature T_{T0} and the static pressure P_1 upstream the probe-induced shock, which need therefore to be measured. Summarizing, total pressure loss assessment through the cascade demands for the concurrent measurements of the inlet total conditions P_{T0}, T_{T0}, of the static pressure downstream the cascade P_1, and of the total pressure at the probe head P_{T2}.

3. Description of the experimental facility

The experimental campaign is designed to be carried out on the Test Rig for Organic VApors (TROVA). The detailed description of the facility and of its operation can be found in [23–25]. The TROVA is a blow-down wind tunnel implementing a batch organic Rankine cycle where a stationary test section replaces the expander. The facility is capable of operating at high non-ideal flow conditions with maximum pressure and temperature of 50 bar and 400 °C respectively, which allow to reach highly non-ideal conditions for a large variety of fluids for ORC applications. Main components of the plant are a 1 m^3 volume high pressure vessel (HPV) where the fluid under scrutiny is charged, typically in two-phase conditions, with a mass defined by the desired test operating conditions in terms of pressure and temperature. To attain test conditions starting from ambient temperature and the related saturation pressure, the fluid is isochorically heated via the external electrical tracing of the HPV and of the pipeline upstream the test section, which is also heated in order to avoid fluid condensation during experimental runs. An insulation layer of the heated portion of the plant strongly limits heat dissipation towards the environment. Once test conditions are reached (several hours are required), the opening of a series of valves starts the test, feeding the test section with organic vapor flow at saturated, superheated, or supercritical conditions. Tests typically last from tens to hundreds of seconds depending on operating conditions and test section passage area, since both affect the discharged mass flow rate. Despite the transient operation, a quasi-steady flow field establishes in the test section which features a characteristic time order of magnitude lower with respect to the HPV emptying process one; also, flow properties are measured with sufficiently high frequency response instrumentation. The vapor exhausted from the test section is discharged into a 6 m^3 volume low pressure vessel (LPV) where it is de-superheated and condensed through a thermal oil heat exchanger, located at the LPV shell and integrated with a cooling tower circuit and a plate oil/water heat exchanger. Finally, a metering pump closes the loop by pumping the liquid working fluid back to the HPV.

4. Design of the experiment

4.1. Operating conditions

All calculations described in the following, including CFD simulations, were performed by applying a state-of-the-art Helmholtz energy equation of state [15] for MM [26], implemented in the NIST RefProp database [27]. Total inlet conditions (station 0 in Fig. 2) in both design and off-design conditions were chosen to carry out expansion processes featuring highly non-ideal fluid thermodynamic states, as pointed out in [22]. The nominal inlet total state (labeled as *DES* in Fig. 3(a)) was

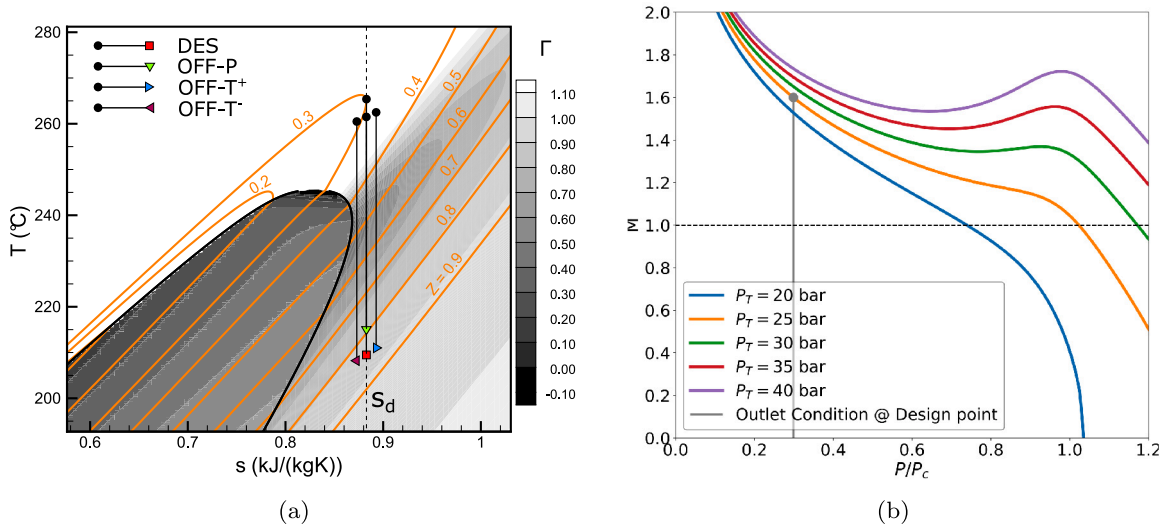

Fig. 3. (a) Temperature - specific entropy per unit mass diagram, with contour of Γ, Z isoline and reference isentropic expansions in both design and off-design conditions for MM vapor. (b) Mach number vs reduced pressure P/P_c distribution for MM vapor isentropic expansions characterized by the same entropy s_d but different stagnation pressure.

computed determining an inlet specific entropy as close as possible to vapor saturation to enhance non-ideal effects along the expansion and to allow the execution of tests in off-design conditions in both temperature and pressure (labels *OFF* in Fig. 3(a)). The design entropy and total pressure were set to $s_d = 0.883$ kJ/(kg K) and $P_{Td} = 25$ bar as shown by line *DES* in Fig. 3(a), which also points out how the expansion crosses a thermodynamic region exhibiting low values of both compressibility factor Z and fundamental derivative of gas dynamics Γ, the latter experiencing also significant gradients. Γ specifies the variation of the speed of sound along isentropic processes [28], and its low values, entailed by high fluid molecular complexity, enhances non-ideal effects with quantitative (and possibly qualitative) impact on the expansion flow field [22]. This choice of conditions allows to widen the explored range of non-ideality within a single test run, while keeping at the same time sufficient safety margin with respect to both test section maximum pressure and fluid thermal stability limit. Fig. 3(b) shows several isentropic expansions for different values of the inlet total pressure and temperature, the latter being computed from P_T and entropy s_d. The expansions show that, increasing the inlet total pressure, non-ideal gasdynamic effects (such as, a Mach number profile departing from the one of an ideal gas) enhance. Therefore, the design inlet total pressure was selected as a compromise between the needs of pointing out flow non-ideality and of safely operate the test section, also at off-design conditions. The corresponding inlet total temperature results equal to 261.5 °C. The outlet static to total pressure ratio, marked with a circle in Fig. 3(b), was chosen to have a high outlet Mach number, typical of high expansion-ratio applications, without relegating the non-ideal effects in a small region close the nozzle throat. The design outlet Mach number was thus set equal to about 1.6, leading to an outlet static pressure of 5.77 bar, computed through one-dimensional theory. Three possible conditions, reported in Fig. 3(a), were identified to investigate cascade off-design performance; the first one, referred to as *OFF-P*, is characterized by a higher inlet total pressure $P_T = 28$ bar and $s = s_d$, while conditions labeled as *OFF-T*$^+$ and *OFF-T*$^-$, consider a higher and lower inlet total temperature (±1 °C) respectively and the design P_{Td}. For such class of off-design conditions non-ideal effects are expected to trigger significant variability in the flow condition, as shown in [22].

4.2. Blade design

A further crucial step in the design of such a novel experiment is the identification of a blade shape optimized for operating in the linear cascade, in terms of thermodynamic condition and cascade set-up. To carry out a tailored blade design, computational fluid dynamics (CFD) was applied, at first to simulate the baseline profile reported in Fig. 2 and then to perform a shape-optimization of the blade. These preliminary design studies where carried out considering a periodic annular row configuration, while further calculations were performed to simulate the flow in the actual linear cascade and to assess the degree of periodicity among adjacent channels, as detailed in Section 4.3. Annular cascade calculations were performed using the CFD flow model developed at Politecnico di Milano for turbomachinery flow simulations, based on the ANSYS-CFX solver, whose formulation specific for supersonic flows of non-ideal gases is fully detailed in [22,29]. The reliability of the numerical model used in this context was previously validated against experiments performed within a research turbine installed at Politecnico di Milano [30]; the model was able to reproduce the detailed aerodynamics and loss mechanisms of the blade rows, and provided estimates of stage efficiency within 1% of the experimental datum, i.e., comparable to the uncertainty of the measurement technique. The same model was also assessed for canonical supersonic flows, such as the shock tube problem and the 2D compression corner [31], providing excellent results in comparison to solutions and/or data. As a further consideration, the suitability of this class of computational set-up for non-ideal flow simulations was also investigated and confirmed in [32]. Simulations were performed considering a quasi-3D slice representative of the midspan section of the cascade. The solver integrates the RANS equations, complemented by the turbulence model equations according to the k-ω SST formulation, by resorting to a look-up table approach to introduce the non-ideal thermodynamics of the fluid. The equations were integrated over structured multi-block meshes composed by about 220,000 hexahedral elements, defined after a dedicated mesh-dependence analysis, whose description and results lie outside the scope of the present work, and by assigning $y^+ \leq 1$ at the blade walls.

Calculations were performed by assigning total pressure, total temperature, flow direction, and turbulence quantities at the inlet, and static pressure at the outlet. The total conditions and the expansion ratio were defined as illustrated in Section 4.1 for the design point (line *DES* in Fig. 3(a)), while the turbulence quantities are assigned following [22]. A dedicated analysis concerning the inlet flow angle was needed since the chosen cascade configuration is quite different from the stator of conventional axial turbines, in which the flow is deflected towards the tangential direction. In this case the blades do not impart any rotation to the flow (as shown in Fig. 2). In a conventional configuration, no flow deflection corresponds to operate the cascade with highly negative incidence, therefore preliminary calculations on

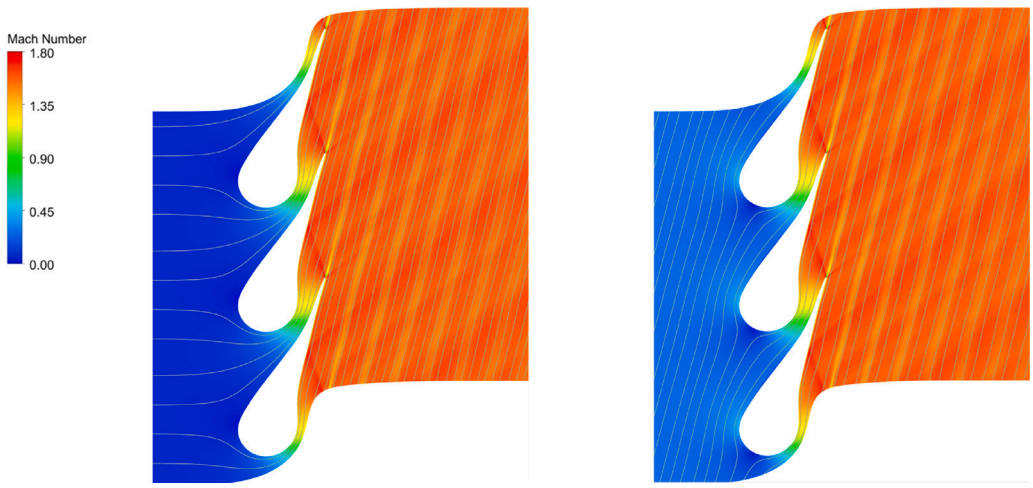

Fig. 4. Mach number field (contour) with overlapped streamlines (gray solid lines). Axial (left) and 75° (right) inlet flow comparison.

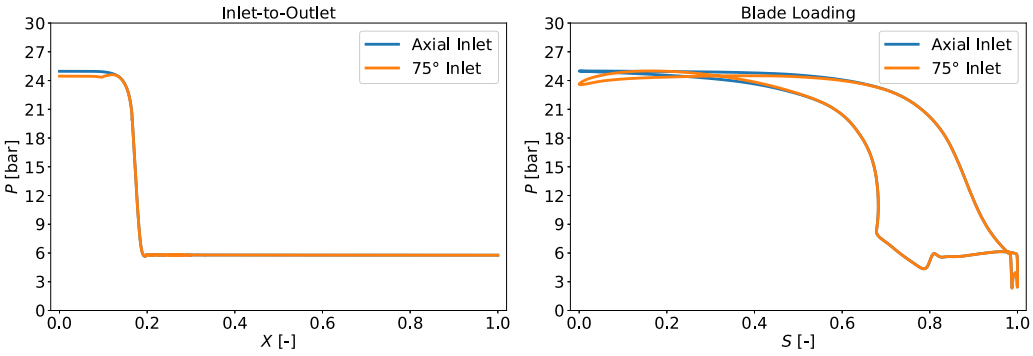

Fig. 5. Axial and 75° inlet flow comparison. Inlet-to-outlet pitchwise mass-averaged pressure distribution (left). Pressure distribution over the blade pressure and suction side (right).

the baseline are required to investigate the effects of such boundary condition, in particular on the post-throat flow evolution. The baseline geometry was numerically analyzed considering the two limiting conditions of inlet flow angle, measured with respect to the annular row axis, equal to 0° (axial inlet flow) and 75° respectively. Despite the mass flow rate is different in the two cases, due to the assignment of the outlet static pressure as boundary condition, the Mach contour reported in Fig. 4 highlights how the two flowfields downstream the sonic throat are almost identical in terms of Mach number value, shock and expansion wave patterns and wake thickness. Obviously, this is not the case of the leading edge region, where the variation of the inlet flow angle leads to different stagnation points, pressure and suction side boundary layers development, and blade pressure distribution. However, thanks to the large radius of curvature at the leading edge, the baseline blade is highly tolerant to the severe change of incidence angle, and no flow detachment is produced. These outcomes are confirmed by the results reported in Fig. 5, in which the blade loading (on the right) and the inlet-to-outlet pitchwise mass-averaged pressure distribution (on the left) are compared for the two cases. The pictures highlight how the differences in terms of blade loading and pressure distribution occur only in the front part of the blade, upstream of the sonic throat. The present comparison corroborates the re-design of the front-section of the blade, with respect to the one described in [22]. By virtue of its peculiar leading edge shape, the present blade is suitable to accept the meridional flow typical of axial machines as well as the highly tangential swirling flow entering stators of radial-inflow turbines. In fact, in radial-inflow turbines the distributor provides a high tangential flow to the nozzle, whose deflection results small and thus close to the one reproduced in the proposed linear cascade experiment.

Even though the baseline blade configuration was already satisfactory, a shape-optimization process was performed to refine the blade shape in the rear part of the channel, especially from the throat section to the outlet, as most of the entropy production in supersonic cascades occurs in this region. The blade design was performed by applying the in-house shape-optimization tool FORMA (Fluid-dynamic OptimizeR for turboMachinery Aerofoils), which optimizes the shape of blade profiles by resorting to surrogate evolutionary strategies, formulated in constrained, multi-point and multi-objective fashion. FORMA, whose details can be found in [29], combines a B-spline representation of the blade profiles, the CFD model previously presented, a Kriging formulation as surrogate, and genetic algorithms. Following the analysis just described, a inlet flow angle of 75° was set as boundary condition. The baseline blade was, at first, parametrized using 30 control points (CPs), and only six of them, covering most of the blade suction side, were considered movable during the optimization process; the mobility of such CPs being the design space of the optimization problem. Fig. 6(a) reports both fixed (red dots) and movable (green dots) CPs, as well as the investigated design space (light green region). In this way, the optimization was addressed to the rear section of the blade, as required. The four CPs defining the trailing edge are kept fixed to concurrently avoid its rigid translation and deformation. The two CPs on the suction side preceding the trailing edge were instead kept fixed to avoid a thinning of the profile, which may lead to non-negligible blade deformations in this region. The global optimization strategy, which was applied for the present optimization problem, involves an initial sampling of the design space for surrogate model interpolation including 60 cascade evaluations, followed by several training iterations that progressively refine the surrogate as the optimization proceeds towards the optimum.

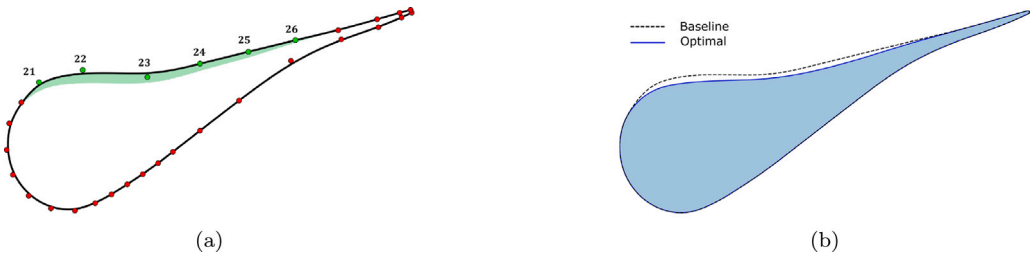

Fig. 6. Blade optimization procedure. (a) Baseline geometry parametrization; red and green dots represent fixed and movable CPs respectively, the light green region represents the design space. (b) Comparison of baseline geometry and optimal blade shape.

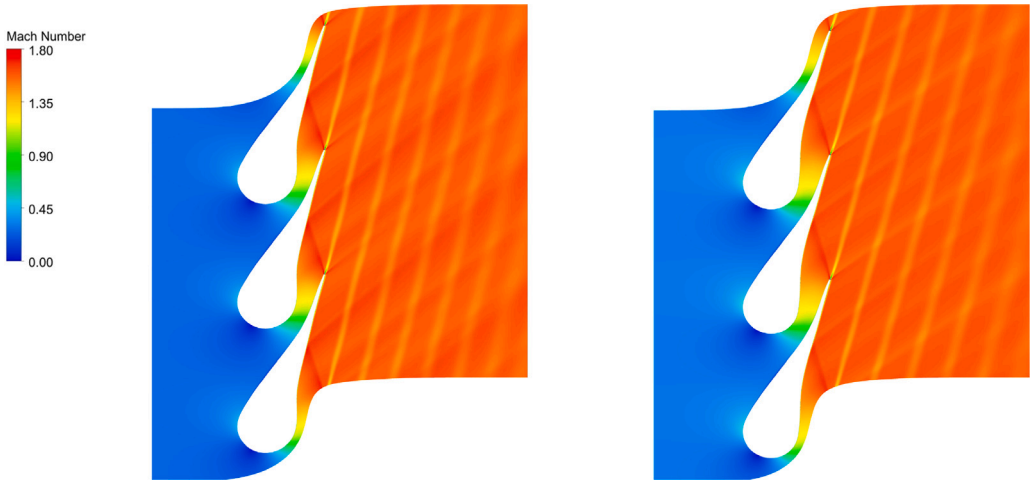

Fig. 7. Mach number field. Baseline (left) and optimal (right) blade comparison.

Table 1
Comparison of baseline geometry with undeformed and deformed optimal blades. Pitchwise mass-averaged flow properties are evaluated at the domain outlet.

	Baseline blade	Optimal blade	Deformed optimal blade
Δs [J/(kg K)]	1.757	1.467	1.468
M [–]	1.569	1.574	1.574
α [deg]	75.8	74	73.95
Y_{tot} %	15.27	12.66	12.67

Additionally, a constrain was imposed to ensure a flow angle at the domain outlet within 74° and 76°, implying a flow deflection within ±1°. The optimization procedure was stopped after 48 iterations of the training phase, leading to 108 total cascade evaluations, since a stable convergence between the surrogate and high-fidelity CFD results was reached. The baseline and optimal blade shapes are compared from a geometrical point of view in Fig. 6(b), while Fig. 7 reports the corresponding Mach fields and Table 1 summarizes the pitchwise mass-averaged values of the main flow properties at the domain outlet for the two configurations. In the table Y_{tot} represents the total pressure loss coefficient, defined as $Y_{tot} = \left(P_{T,up} - P_{T,dn}\right) / \left(P_{T,dn} - P_{dn}\right)$, with subscript up and dn referring to upstream and downstream blade conditions respectively. Besides the outlet Mach number is slightly higher, the optimal blade is characterized by lower Mach number values within the supersonic diverging portion of the channel. This contributes to prove that in the optimal configuration the flow undergoes a milder pressure drop up to the design outlet one, leading to weaker fishtail shocks and, consequently, to lower entropy production and total pressure losses, as highlighted in Table 1 by the values of Δs and Y_{tot}.

Since the optimal blade (as well as the baseline one) is characterized by a very thin tail, being the thickness lower than 3 mm for a non-negligible portion of the profile up to 0.5 mm at the trailing edge, its structural integrity and the expected deformation due to the blade loading have been assessed by means of finite element method analyses (FEM). FEM simulations were performed using the Abaqus/CAE solver, a module of Abaqus FEA software [33]. The pressure distribution retrieved from CFD results was imported in the software and applied as an external load acting on the blade surface, while the geometry was fixed according to the actual dowel-clamping mechanism employed in the experiment. The resulting maximum stress turned out to be much lower than the material yielding limit, while the maximum deformation was found to be of about 0.1 mm. To investigate the effect of the blade deformation on the resulting flow-field downstream the throat section, the deformed blade geometry was numerically investigated in annular cascade configuration, exploiting the same numerical set-up previously described. The results, in terms of pitchwise mass-averaged flow properties at the domain outlet, are reported in Table 1, where they are compared to those of the baseline and of the optimal undeformed blade. Clearly, the deformation field caused by the blade pressure distribution does not produce any remarkable variation on the resulting flow-field. Therefore, the loss reduction attained by the optimization process is not compromised, which proves the effectiveness of the design process.

4.3. Cascade design

The linear cascade implements three complete blades featuring the optimized profile and arranged horizontally to attain a stagger angle $\alpha_s = 75°$ as illustrated in Figs. 2 and 8(a). The blade row is then completed by partial pressure side (bottom right in Fig. 8(a)) and suction side (top left in Fig. 8(a)) profiles, integrated into two side-walls bounding the flow field upstream and downstream the cascade. Fig. 8(a) reports also the downstream measuring grid (red points), whose definition procedure is reported in the following, and the position of the in-channel static pressure taps (yellow labeled dots). To attain a high level of periodicity and to minimize disturbances at the measuring points due to fishtail shocks departing from trailing edges

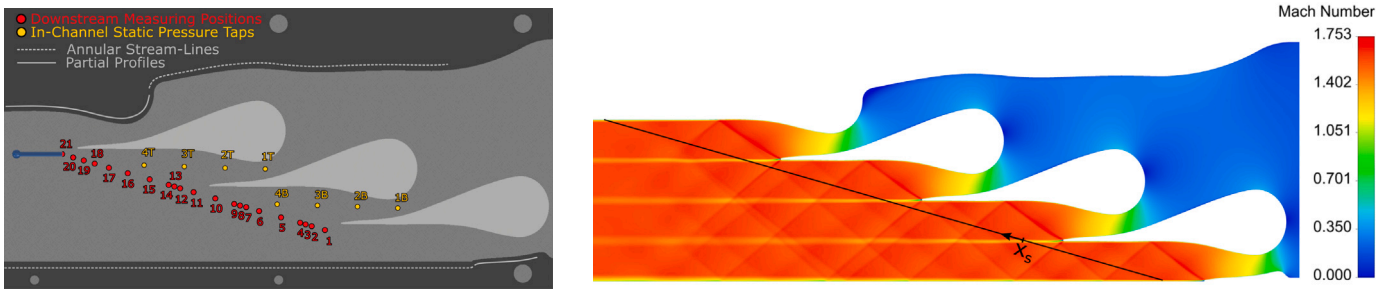

Fig. 8. Full linear cascade. (a) Final arrangement including side-walls design details and measurement points. The total pressure probe is also shown. (b) Two-dimensional CFD simulation results: Mach Field.

and their reflections, the design of side-walls was carried out reproducing the flow streamlines simulated in the annular row configuration (see Fig. 8(a)). The front part of the side-walls is properly shaped to smoothly connect with the inlet duct.

The periodicity of the flow was verified through CFD investigations of the full cascade geometry. Simulations were performed by means of the ANSYS-Fluent solver, considering a 2D numerical domain representative of the midspan section of the cascade. Although the same CFD flow model detailed in Section 4.2 was exploited (i.e., RANS equations complemented by the k-ω SST turbulence model and by look-up tables to introduce the thermophysical properties of the fluid), these simulations were run with ANSYS-Fluent thanks to the possibility of performing 2D simulations and thus saving computational costs and time. Preliminary comparisons were however made between the two solvers for both the annular and linear cascade configurations, finding full qualitative and quantitative correspondence between the results obtained. The equations were integrated over structured multi-block meshes created with ANSYS-ICEM CFD and composed by about 345,000 hexahedral elements. The mesh dimension was chosen after a dedicated mesh-dependence analysis, whose description and results lie outside the scope of the present work, and by keeping constant the near-wall distance ($y^+ \leq 1$). Differently from the physical one, the numerical domain implements inlet and outlet mesh blocks extending upstream and downstream for about 0.75 and 5 blade chords respectively. Since the flow streamwise Mach number is supersonic, calculations were performed by assigning at the inlet total pressure and temperature, flow direction, and turbulence. To assess cascade periodicity, inlet conditions were set accordingly to the experiment design point, that is $T_t = 261.5$ °C and $P_t = 25$ bar, while the inlet flow was considered parallel to blade stagger, and the turbulence quantities are provided according to [22].

The numerical simulation results are shown in Fig. 8(b) in terms of Mach number field. The Mach distribution provides a first proof of the good periodicity of the downstream flow-field, being the reflection waves generated at the bottom side-wall the major source of non-periodicity. Fig. 8(b) also reports (in black) the measuring line, parallel to the trailing edge locus at a distance of 17% of the blade chord (see also Figs. 2). To define the measuring point position the Mach field reported in Fig. 8(b) and the corresponding total pressure distribution were exploited. The downstream measuring grid results non-uniformly spaced, but conveniently refined in the vicinity of the wakes where higher gradients are expected, as shown in Fig. 8(a).

The numerical results over the black line of Fig. 8(b) were extracted to thoroughly investigate the downstream flow-field periodicity, as shown in the example reported in Fig. 9(a), in which the Mach number distribution over the measuring line is plotted against the non-dimensional pitch-wise distance x_s from the bottom blade trailing edge (see Fig. 8(b)). Fig. 9(a) also depicts the position of the measuring points. The autocorrelation function was applied to the distribution over the measuring line of the most relevant flow properties (such as the Mach number, reported in Fig. 9(a)) to assess the degree of overlapping of the various signals with their delayed copies as function of the delay. This analysis highlighted that the fluid dynamic pitch is almost identical to the 45 mm geometrical one, with a deviation lower than 0.6 mm ($\approx 1.3\%$ of the pitch) independently of the physical flow property considered. In particular, for relevant flow properties – such as the entropy rise or the total pressure – the non-dimensional auto-correlation function resulted equal to about 0.97 for the points of maximum overlapping. These outcomes confirm the remarkable flow-field periodicity obtained, which is further emphasized by the results reported in Fig. 9(b), in which the suction and pressure side pressure distributions related to the three full blades is reported.

Since the TROVA facility operates as blow-down wind tunnel, total conditions at cascade inlet are continuously changing as the HPV empties. Therefore, the full cascade was also tested at several off-design conditions by means of CFD simulations implementing the numerical set-up already described, but with different inlet conditions. A discrete number of calculations were performed by varying P_t from 25 bar to 5 bar and T_t from 261.5 °C to 230.3 °C, following a typical HPV emptying curve, as found in [34]. This analysis was carried out mainly to assess the flow-field periodicity throughout the whole experiment as well as to exclude the occurrence of phenomena that may bring to misleading measurements, such as separations or unexpected shock patterns. The results of the off-design analysis are summarized in Fig. 10, in which the Mach number distribution along the measuring line is reported for different inlet total conditions, representing the whole set of off-design operations numerically tested. The Mach number increases as the total pressure reduces and more ideal conditions are attained, as foreseen by theory and proven experimentally in [16]. Even though the flow-field varies as the HPV is emptying, periodicity remains extremely satisfactory, as depicted in Fig. 10 and confirmed by an autocorrelation-based analysis that revealed a difference between the fluid-dynamic and geometrical pitches always lower than 1.5 mm ($\approx 3.3\%$ of the pitch) for most relevant flow properties.

4.4. Test section arrangement

According to the design procedures described above, the cascade implements three complete blades and two side-walls, as shown in Fig. 11, in which the final cascade arrangement and the Mach field resulting from 2D CFD simulation are overlapped. The flow delivered by two complete blade channels, including three wakes, is expected to be available for downstream characterization. The cascade is closed on the front and rear side through planar end-walls. On the rear steel plate, blades and sidewalls are dowel-fixed and pressure taps and instrument accesses are machined. The plate is mirror polished and the front end-wall is made by a quartz window, allowing schlieren visualization in double-passage configuration. Main dimensions characterizing the cascade are a pitch of 45 mm, a blade chord of 66.5 mm, and a blade height of about 19 mm. The passage throat width in the blade-to-blade plane is approximately 5.5 mm.

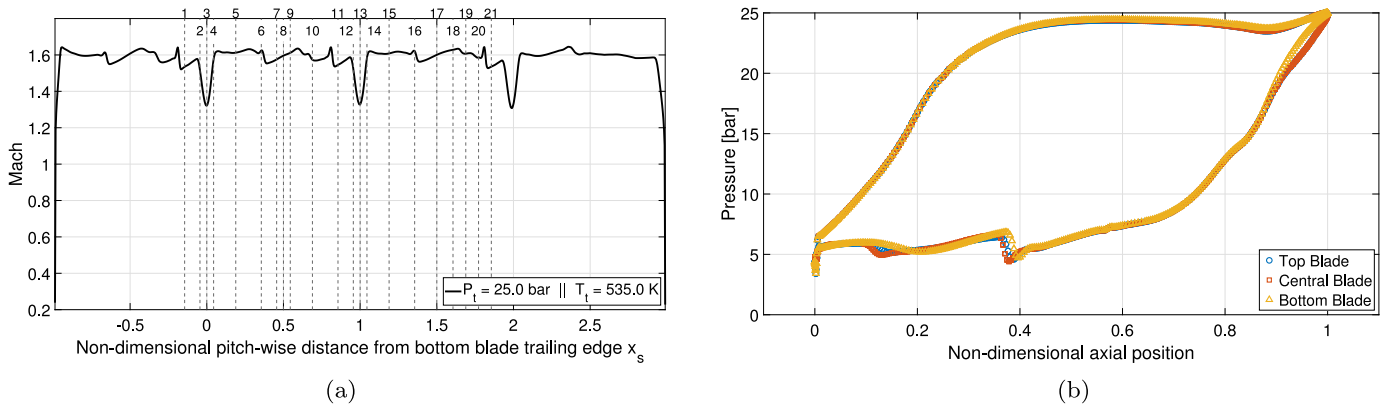

Fig. 9. Periodicity analysis results. (a) Mach distribution over the measuring line and vertical dashed lines representing measuring points position. (b) Suction and pressure side pressure distributions related to the three complete blades.

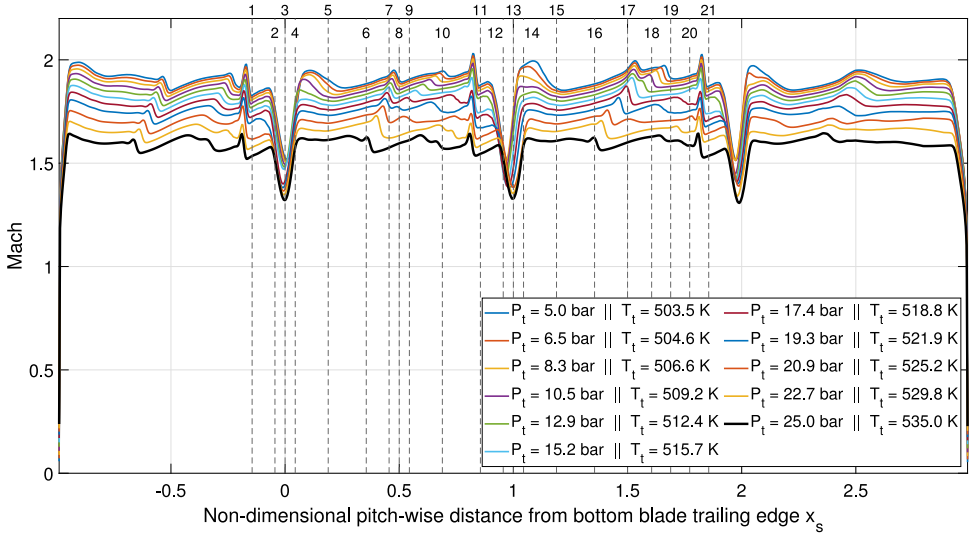

Fig. 10. Mach distribution over the measuring line for design and off-design conditions. Vertical dashed lines indicate measuring points position.

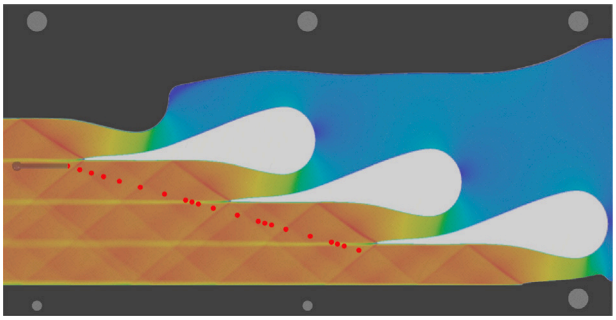

Fig. 11. Test section as resulting from design including side-walls, total pressure probe and downstream measurement points.

The cascade inlet flow comes from a settling chamber (plenum) upstream the test section, with a moderate and smooth acceleration and it is therefore considered uniform. Also, the action of heating system and of insulation on plenum and test section allows to consider the flow adiabatic. Therefore, total condition T_{T0}, P_{T0} are measured within the settling chamber. Total temperature is provided by two thermocouples (of J and K type) with expanded uncertainty of 1 °C. Due to the negligible kinetic energy in the plenum, the total pressure is measured by a wall flush-mounted absolute piezoresistive transducer for high-temperature applications; the expanded uncertainty is approximately 0.1% of the full scale (FS). Due to the inevitable non-uniformity, the downstream flow characterization requires a measurement traversing; a measuring grid parallel to the trailing edge locus was therefore designed, as previously described. The grid features 21 points not uniformly spaced along the two central blade pitches (see Fig. 11). Along this line, the 1.5 mm diameter head of a total pressure probe, pre-aligned with the flow and featuring a recessed stem, is located at different points, which constitute the measuring grid where pressure P_{T2} is measured. The probe head is located at blade mid-span, while at the rear wall, static pressure taps of 0.3 mm diameter are machined at the same positions along the whole measuring grid to retrieve pressure P_1. This is possible thanks to the bowed shape of the probe-induced shock and to the two-dimensional nature of the flow. The total pressure probe access is machined in the steel back plate, as well as the required sealing and rotation/blade-span translation system. Thanks to an already proven test repeatability [34], the probe traversing is obtained with multiple test runs, with one single measuring point accessed at each run. This extends the experimental campaign duration, but entails two indubitable advantages. The first one is to simplify the implementation of the sealing system, since no pitch-wise probe movement is required. The second one is the chance of exploring a wide range of operating conditions in a single test, from highly non-ideal to almost ideal, during the HPV emptying. The measuring system

is complemented by two rows of four static pressure taps arranged at the end-wall plate, along the centerline of the diverging portion of the two central channels (see green dots in Fig. 8(a)). Moreover, a double-passage schlieren equipment is available to visualize the flow field density gradients, highlighting the morphology of shock/fan waves originated at blade trailing edges and at the probe head with an almost continuous space resolution. These further measurements implemented will provide crucial information and data relevant for CFD development and validation. All static pressure taps are connected with pneumatic lines, embedded in the heated back plate, to absolute piezoresistive pressure transducer for high temperature, exhibiting 0.1% FS expanded uncertainty. No condensation issues arise, but sensitivity to temperature requires transducers calibration in both pressure and temperature. Contrarily, the total pressure P_{T2} is measured using P_{T0} as reference, via a differential pressure transducer (of 0.05% FS expanded uncertainty) aiming at minimizing uncertainty on loss quantification. Such sensors are for low temperature applications and thus remotely mounted. Therefore, the related pneumatic lines need to be flushed with nitrogen, in order to avoid line condensation and the consequent unacceptable promptness reduction, see [35] for details.

5. Early experimental tests

Preliminary experiments were performed without the total pressure probe and exploiting MM as working fluid. These tests target total pressure and temperature at the cascade inlet equal to $P_T = 18$ bar $T_T = 243.5$ °C respectively, leading to an initial compressibility factor at the cascade inlet equal to about 0.47. This allows to span a wide range of inlet non-ideal conditions since Z tends to increase during a single test run, as the HPV emptying process proceeds, up to reach almost ideal conditions ($Z \approx 1$) at the end of the test. In particular, these preliminary experiments and the corresponding results hereinafter reported, aim at proving the effectiveness of the cascade design in representing the actual flow-field developing in the bladed and semi-bladed regions of supersonic ORC nozzle vanes, both in terms of shock/fan patterns and of periodicity. In Fig. 12 two schlieren images acquired at different time instants are reported, together with a map of the taps corresponding to the acquired and processed pressure signals. The left-side frame corresponds to $P_T = 8.63$ bar and $Z = 0.78$ (test midpoint), while the right-sided one to $P_T = 3.09$ bar and $Z = 0.93$ (final part of the experiment). Both the images clearly show the fishtail shocks departing from bottom and central blades, as well as the wave patterns developing within the diverging portion of middle and top channels. Focusing on the left frame, the dark regions upstream and within the throat highlight a combination of large density values and gradients such that the schlieren laser beam deflection is beyond the measuring range. In fact, such regions correspond to the stagnation point and to high-acceleration dynamics occurring in the first part of the pressure side and through the throat respectively. Another interesting aspect is the variation of the fishtail opening angle, which tend to rotate downstream with an increasing leaning as the test proceeds, as can be inferred referring to shock position with respect to pressure taps marked as 3T and 3B in the two frames of Fig. 12. This phenomenon is due to a progressive increase of the Mach number at blade channel outlet, just upstream the fishtail shock, related to the reducing non-ideality along the test. This is an expected behavior, as confirmed by the computed Mach distributions reported in Fig. 10.

Being interested in validating the flow field developing within the bladed channels, the signals retrieved from the three upstream pressure taps (1B, 2B, 3B, 1T, 2T, and 3T) were processed to investigate cascade periodicity and effectiveness of numerical simulations in representing actual experimental results. The acquired static pressures are reported in Fig. 13 for both the channels as function of the test running time, providing a direct assessment of attained periodicity and a representative example of typical blow-down wind tunnel emptying dynamics, characterized by slowly reducing pressure levels. As highlighted in Fig. 13, the pressure signals acquired by taps 1T/1B and 2T/2B exhibit a very good periodicity, being the lower and upper channel pressures always almost overlapped. On the contrary, the signals acquired by taps 3B and 3T present larger discrepancies for most of the test run, up to about 60 s. This difference can be explained by a non-perfect periodicity between the two central channels, leading to a slightly different slope of the fishtail shocks, especially those stemming from the blade pressure side and directed towards adjacent blade suction side. In fact, as shown in Fig. 12, the fishtail shock branches enter the channels position very close to the respective 3B and 3T taps, in a region characterized by very large pressure gradients, such that even a small variation of the tap-shock distance produces a considerable variation of the measured pressure. In particular, as confirmed by left and right frames in Fig. 12, the upper channel tap (3T) lies just upstream the shock throughout the test duration, justifying the regular signal plotted in Fig. 13, as well as lower initial pressure. On the contrary, in the lower channel the fishtail shock oversteps tap 3B as the test proceeds, moving from a larger measured pressure at the beginning of the test (shock overlapped to tap 3B, left frame in Fig. 12), to pressure values lower than those measured by tap 3T when the shock passes beyond tap 3B. When the distance between the shock and tap 3B increases enough (right frame in Fig. 12) to let the tap outside the high-pree gradient region associated to the shock, the discrepancies between the two signals largely reduce (as depicted in Fig. 13 starting from about 60 s), as the pressure at that point becomes essentially a function of the geometric area ratio.

Finally, the pressures retrieved by the first three upstream taps are compared with numerical simulation results in Fig. 14. In particular, two time instants are considered; the one for which the measured inlet total pressure and temperature are, respectively, $P_T = 8.63$ bar and $T_T = 224.8$ °C (left frame in Fig. 12) and the one for which $P_T = 3.09$ bar and $T_T = 216.4$ °C (right frame in Fig. 12). The boundary conditions for the two numerical simulations are set accordingly, still exploiting the same numerical schemes and settings described in Section 4.2. The pressure values numerically computed are reported in Fig. 14 together with the related error-bars that take into account the pressure variation over a circle with a radius of 0.3 mm (equal to the one of the manufactured taps). The results highlighted in Fig. 14 depicts an outstanding agreement between measured and computed pressure values within the diverging portion of both the two central bladed channels, with the only exception of tap 3B for the high-pressure case. This larger, though still acceptable, discrepancy is due to a non-perfect prediction of the fishtail opening angle, which in the experiments result slightly more rotated upstream with respect to the one predicted by numerical simulations. Such mismatch concerning the fishtail leaning is however enough to produce appreciable differences between measured and computed pressure values, since tap 3B results very close to the pressure side fishtail and, consequently, in a region of high pressure gradients as already detailed before. It is worth noting that such effects are amplified as test conditions depart from those employed for cascade design, since off-design conditions make the flow field at the trailing edge more complex to be simulated.

The outcomes of these preliminary experiments – without the probe and focused on the investigation of the flow-field within the bladed channels – are encouraging since they prove the effectiveness of the designed linear cascade in reproducing shock patterns typical of actual supersonic stators of ORC turbines with a good periodicity level between the two central channels. Moreover, the agreement with CDF simulations confirm that such numerical tool can be exploited both in the design phase of ORC turbines and as benchmark to validate the results of following experiments.

6. Conclusions

The design of an innovative experiment on linear supersonic ORC blade cascade to be carried out on the TROVA facility at Politecnico di Milano is described in this paper. The planned campaign aims at

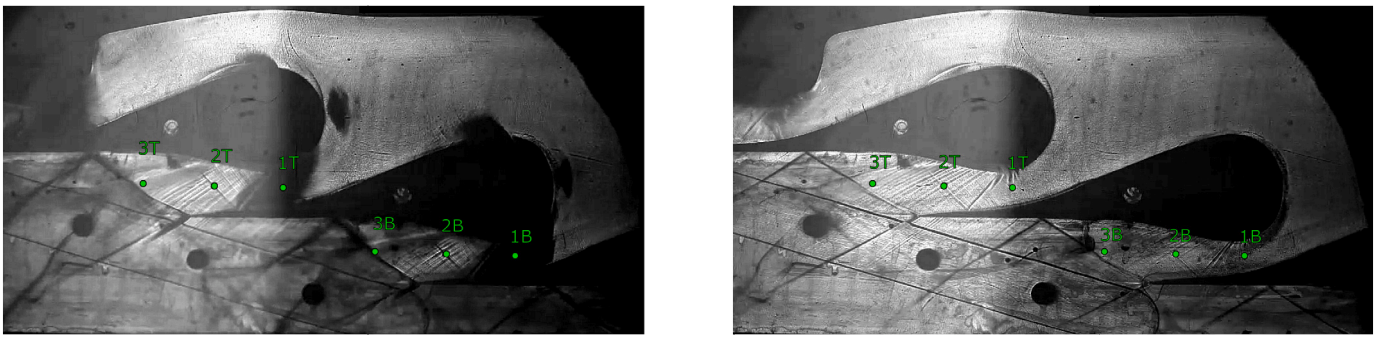

Fig. 12. Schlieren images acquired at different time instants: (left) test midpoint, $P_T = 8.63$ and $Z = 0.78$, (right) final part of the experiment, $P_T = 3.09$ and $Z = 0.93$.

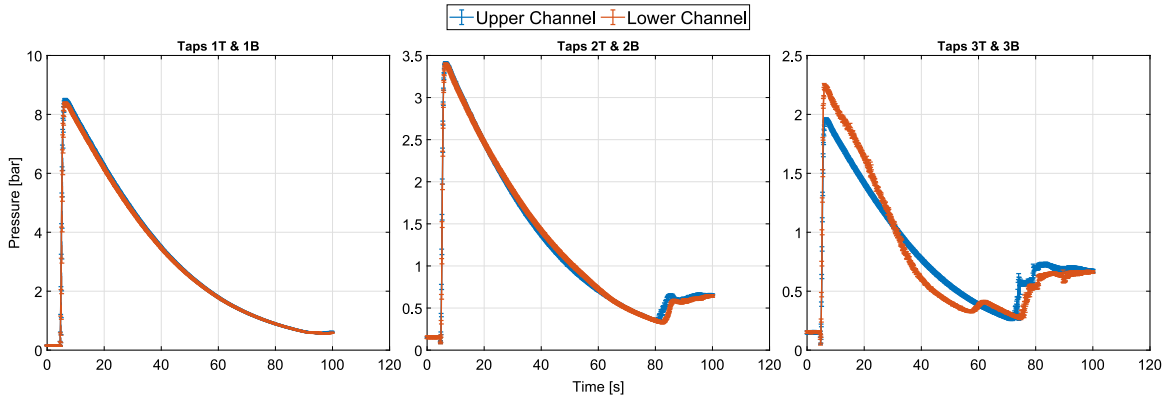

Fig. 13. Comparison between pressure signals acquired by upper and lower channel pressure taps: tap 1B *vs* tap 1T, tap 2B *vs* tap 2T, and tap 3B *vs* tap 3T.

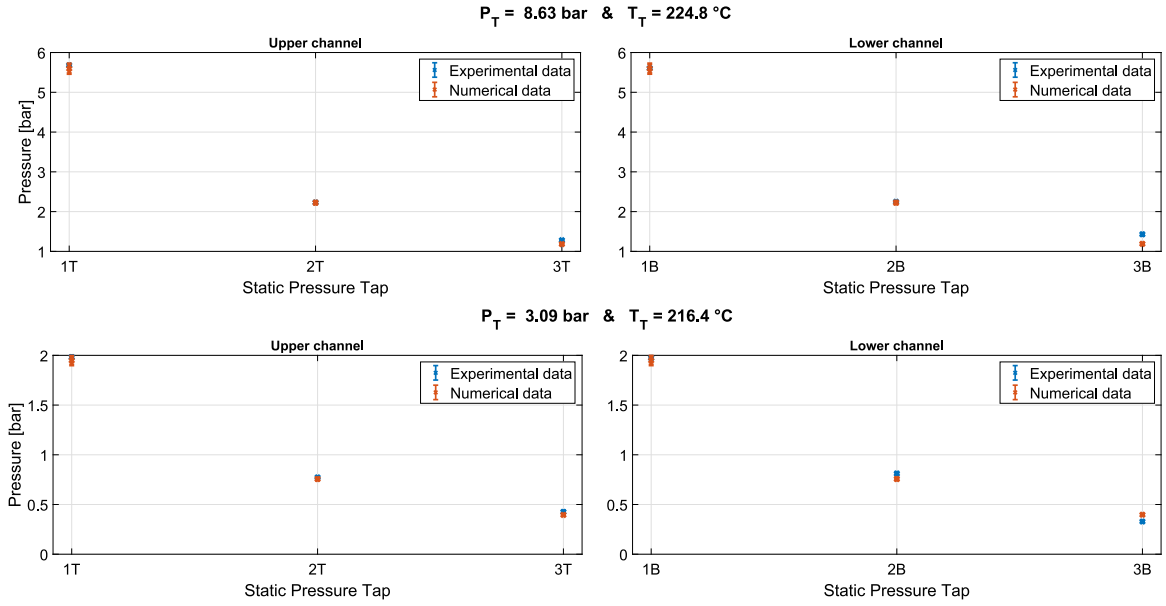

Fig. 14. Comparison between measured and numerical static pressures at positions 1B, 1T, 2B, 2T, 3B, and 3T, for two different time instants: (top) test midpoint, $P_T = 8.63$ and $Z = 0.78$, (bottom) final part of the experiment, $P_T = 3.09$ and $Z = 0.93$.

providing relevant experimental data for development and validation of high-fidelity CFD-based tools currently employed for ORC turbine design, optimization and analysis. A planar cascade arrangement resembling a typical supersonic ORC stator blade row was devised and implemented. To comply with space and geometry constraints dictated by the current facility arrangement, a row of three blades plus two sidewalls was designed to attain null deflection of the incoming flow and a stagger angle of 74°. Such arrangement is found to be representative of supersonic stator blades for both axial and radial inflow stages. The cascade was designed and optimized by exploiting 2D CFD simulations to operate with siloxane MM at a specific design condition. The side walls tailored design allowed to attain a very good flow periodicity in both design and off-design conditions, the latter being required since tests are foreseen at largely variable operating conditions, from highly non-ideal states to almost ideal gas conditions. Dedicated FEM analyses revealed negligible deformation of the blade trailing edge region under

the developed pressure loads. The devised measuring system includes an L-shaped total pressure probe and a wall static pressure tap, required to retrieve the total pressure downstream the cascade (thus upstream the probe-induced bowed shock), and eight in-channel static pressure taps exploited to measure the end-wall pressure distribution within the divergent portion of the two central blade channels. A traversing system covering two full blade pitches was also conceived for the total pressure probe, which allows to measure total pressure losses downstream the cascade with a spatial resolution as high as the one required for CFD validation, especially in the high-gradient locations as the wake region. Schlieren visualizations were also arranged to highlight the trailing edge flow configuration, which significantly contributes to cascade losses. These visualizations, combined with in-channel pressure measurements, are crucial for supporting the interpretation of the experimental results as well as for the development of proper flow models for numerical simulations.

Finally, a set of preliminary experiments was performed by expanding MM vapor within the designed cascade at thermodynamic states typical of ORC applications. Two different operating conditions, featuring significant ($Z \approx 0.78$) and low ($Z \approx 0.93$) level of non-ideality were analyzed with the twofold aim of proving the suitability of the cascade of reproducing the actual flow field in bladed and semi-bladed channels of supersonic ORC vanes and of assessing the capability of design/analysis CFD tools of simulating such flow field. Tests results confirmed the development within the cascade of the typical flow occurring within ORC annular rows, in terms of shock/fan patterns and periodicity, as well as its dependence on the level of non-ideality. Moreover, comparisons of CFD simulations with the experiments showed excellent agreement, thus assessing the validity of the theoretical tools applied in the design phase and the suitability of the employed CFD models for the design and the analysis of ORC turbines.

Considering the novelty of such experiments, their design, in terms of both test section arrangement and development of suitable measurement techniques, is described in detail in this paper with the purpose of serving as a reference for further investigation on ORC turbine flows, capable of providing reliable experimental data which are still scarce in the open literature.

Declaration of competing interest

The authors declare the following financial interests/personal relationships which may be considered as potential competing interests: Andrea Spinelli reports financial support was provided by Government of Italy Ministry of Education University and Research.

Data availability

The data that has been used is confidential.

Acknowledgments

This research is part of the Energy for Motion project of the Department of Energy of Politecnico di Milano, funded by the Italian Ministry of University and Research (MUR) through the Department of Excellence grant 2018–2022. The authors are grateful to both the Ministry and the Department. The authors also wish to thank Professor Alberto Guardone, director of the CREA laboratory where the experimental campaign is taking place, and Gianluca Garosio and Marco Oliveti to their relevant contribution to the research activities here reported.

References

[1] P. Colonna, E. Casati, C. Trapp, T. Mathijssen, J. Larjola, T. Turunen-Saaresti, A. Uusitalo, Organic Rankine cycle power systems: From the concept to current technology, applications, and an outlook to the future, J. Eng. Gas Turbines Power 137 (2015).

[2] E. Macchi, M. Astolfi, Organic Rankine Cycle (ORC) Power Systems. Technologies and Applications, in: Woodhead Publishing Series in Energy: Number 107, Elsevier, New York, 2017.

[3] A. Glassman, Enhanced Analysis and Users Manual for Radial-inflow Turbine Conceptual Design Code RTD, Technical Report, NASA-Contractor Report CR-195454, Washington D.C., USA, 1995.

[4] C.A.M. Ventura, P.A. Jacobs, A.S. Rowlands, P. Petrie-Repar, E. Sauret, Preliminary design and performance estimation of radial inflow turbines: An automated approach, J. Fluids Eng. 134 (3) (2012) http://dx.doi.org/10.1115/1.4006174.

[5] A. Meroni, M. Robertson, R. Martinez-Botas, F. Haglind, A methodology for the preliminary design and performance prediction of high-pressure ratio radial-inflow turbines, Energy 164 (2018) 1062–1078.

[6] A. La Seta, A. Meroni, J.G. Andreasen, L. Pierobon, G. Persico, F. Haglind, Combined turbine and cycle optimization for organic Rankine cycle power systems—Part B: Application on a case study, Energies 9 (6) (2016) 393.

[7] M.T. White, A.I. Sayma, Simultaneous cycle optimization and fluid selection for ORC systems accounting for the effect of the operating conditions on turbine efficiency, Front. Energy Res. 7 (2019) 50.

[8] D. Ainley, G.C. Mathieson, A Method of Performance Estimation for Axial-Flow Turbines, Technical Report, Aeronautical Research Council London (United Kingdom), 1951.

[9] M. Vavra, Axial flow turbines, in: Von Karman Institute for Fluid-Dynamics, Lecture Series 15, 1969.

[10] H.R.M. Craig, H.J.A. Cox, Performance estimation of axial flow turbines, Proc. Inst. Mech. Eng. 185 (1) (1970) 407–424.

[11] A. Glassman, Computer Program for Design Analysis of Radial-Inflow Turbines, Technical Report, NASA Technical Note, TN D-8164, Washington D.C., USA, 1976.

[12] N.C. Baines, I. of Mechanical Engineers, C.E. Group, A meanline prediction method for radial turbine efficiency, Turbocharging Air Manage. Syst. (11) (1998) 45–56.

[13] D. Fiaschi, G. Manfrida, F. Maraschiello, Thermo-fluid dynamics preliminary design of turbo-expanders for ORC cycles, Appl. Energy 97 (2012) 601–608.

[14] C.M. De Servi, M. Burigana, M. Pini, P. Colonna, Design method and performance prediction for radial-inflow turbines of high-temperature mini-organic Rankine cycle power systems, J. Eng. Gas Turbines Power 141 (9) (2019).

[15] R. Span, W. Wagner, Equations of state for technical applications. I. Simultaneously optimized functional forms for nonpolar and polar fluids, Int. J. Thermophys. 24 (1) (2003) 1–39.

[16] A. Spinelli, G. Cammi, S. Gallarini, M. Zocca, F. Cozzi, P. Gaetani, V. Dossena, A. Guardone, Experimental evidence of non-ideal compressible effects in expanding flow of a high molecular complexity vapor, Exp. Fluids 59 (126) (2018).

[17] M. Robertson, P. Newton, T. Chen, R. Martinez-Botas, Development and commissioning of a blowdown facility for dense gas vapours, in: Proceedings of the ASME Turbo Expo, vol. 3, 2019, http://dx.doi.org/10.1115/GT2019-91609.

[18] F. Beltrame, A. Head, C. De Servi, M. Pini, F. Schrijer, P. Colonna, First experiments and commissioning of the ORCHID nozzle test section, ERCOFTAC Ser. 28 (2021) 169–178, http://dx.doi.org/10.1007/978-3-030-69306-0_18.

[19] M. Zocca, A. Guardone, G. Cammi, F. Cozzi, A. Spinelli, Experimental observation of oblique shock waves in steady non-ideal flows, Exp. Fluids 60 (101) (2019).

[20] F. Reinker, R. Wagner, L. Hake, S. der Wiesche, High subsonic flow of an organic vapor past a circular cylinder, Exp. Fluids 62 (3) (2021) http://dx.doi.org/10.1007/s00348-021-03158-y.

[21] D. Baumgärtner, J. Otter, A. Wheeler, The effect of isentropic exponent on transonic turbine performance, in: Proceedings of the ASME Turbo Expo, vol. 2C-2019, 2019, http://dx.doi.org/10.1115/GT2019-90251.

[22] A. Romei, D. Vimercati, G. Persico, A. Guardone, Non-ideal compressible flows in supersonic turbine cascades, J. Fluid Mech. 882 (2020) A121–A1226, http://dx.doi.org/10.1017/jfm.2019.796.

[23] A. Spinelli, V. Dossena, P. Gaetani, C. Osnaghi, D. Colombo, Design of a test rig for organic vapours, in: Proceedings of ASME Turbo Expo, Glasgow, UK, 2010.

[24] A. Spinelli, M. Pini, V. Dossena, P. Gaetani, F. Casella, Design, simulation, and construction of a test rig for organic vapors, J. Eng. Gas Turbines Power 135 (2013).

[25] M. Pini, A. Spinelli, V. Dossena, P. Gaetani, F. Casella, Dynamic simulation of a test rig for organic vapours, in: ASME 2011 5th International Conference on Energy Sustainability, ES 2011, no. PARTS A, B, AND C, 2011, pp. 1977–1988, http://dx.doi.org/10.1115/ES2011-54212.

[26] M. Thol, F.H. Dubberke, G. Rutkai, T. Windmann, A. Köster, R. Span, J. Vrabec, Fundamental equation of state correlation for hexamethyldisiloxane based on experimental and molecular simulation data, Fluid Phase Equilib. 418 (2016) 133–151.

[27] E.W. Lemmon, I.H. Bell, M.L. Huber, M.O. McLinden, NIST Standard Reference Database 23: Reference Fluid Thermodynamic and Transport Properties-REFPROP, Version 10.0, orgname=National Institute of Standards and Technology, 2018, https://doi.org/10.18434/T4/1502528, URL: https://www.nist.gov/srd/refprop.

[28] P.A. Thompson, A fundamental derivative in gasdynamics, Phys. Fluids 14 (9) (1971) 1843–1849.

[29] G. Persico, P. Rodriguez-Fernandez, A. Romei, High-fidelity shape optimization of non-conventional turbomachinery by surrogate evolutionary strategies, J. Turbomach. 141 (8) (2019).

[30] P. Gaetani, G. Persico, Influence of the rotor-driven perturbation on the stator-exit flow within a high-pressure gas turbine stage, Int. J. Turbomach. Propuls. Power 6 (3) (2021) 28.

[31] N. Mushtaq, G. Colella, P. Gaetani, Design and parametric analysis of a supersonic turbine for rotating detonation engine applications, Int. J. Turbomach. Propuls. Power 7 (1) (2022) 1.

[32] M. Pini, S. Vitale, P. Colonna, G. Gori, A. Guardone, T. Economon, J. Alonso, F. Palacios, SU2: the open-source software for non-ideal compressible flows, J. Phys.: Conf. Ser. 821 (1) (2017) 012013.

[33] M. Smith, ABAQUS/Standard User's Manual, Version 6.9, Dassault Systèmes Simulia Corp, United States, 2009.

[34] G. Cammi, C. Conti, A. Spinelli, A. Guardone, Experimental characterization of nozzle flow expansions of siloxane MM for ORC turbines applications, Energy 218 (2021).

[35] C.C. Conti, A. Fusetti, A. Spinelli, P. Gaetani, A. Guardone, Pneumatic system for pressure probe measurements in transient flows of non-ideal vapors subject to line condensation, Measurement (2022) 110802, https://doi.org/10.1016/j.measurement.2022.110802.